materials

MDPI

Article

Structure and Photoluminescence Properties of Thermally Synthesized V_2O_5 and Al-Doped V_2O_5 Nanostructures

Chih-Chiang Wang [1], Chia-Lun Lu [2], Fuh-Sheng Shieu [1,*] and Han C. Shih [1,2,*]

[1] Department of Materials Science and Engineering, National Chung Hsing University, Taichung 40227, Taiwan; wilbur0913@gmail.com
[2] Department of Chemical Engineering and Materials Science, Chinese Culture University, Taipei 11114, Taiwan; ken.lu1988@gmail.com
* Correspondence: fsshieu@dragon.nchu.edu.tw (F.-S.S.); hcshih@mx.nthu.edu.tw (H.C.S)

Abstract: Al-free and Al-doped V_2O_5 nanostructures were synthesized by a thermal-chemical vapor deposition (CVD) process on Si(100) at 850 °C under 1.2 × 10^{-1} Torr via a vapor-solid (V-S) mechanism. X-ray diffraction (XRD), Raman, and high-resolution transmission electron microscopy (HRTEM) confirmed a typical orthorhombic V_2O_5 with the growth direction along [110]-direction of both nanostructures. Metallic Al, rather than Al^{3+}-ion, was detected by X-ray photoelectron spectroscopy (XPS), affected the V_2O_5 crystallinity. The photoluminescence intensity of V_2O_5 nanostructure at 1.77 and 1.94 eV decreased with the increasing Al-dopant by about 61.6% and 59.9%, attributing to the metallic Al intercalated between the V_2O_5-layers and/or filled in the oxygen vacancies, which behaved as electron sinks. Thus the Al-doped V_2O_5 nanostructure shows the potential applications in smart windows and the electrodic material in a Li-ion battery.

Keywords: Al-doped V_2O_5 nanostructures; photoluminescence; vapor-solid mechanism

Citation: Wang, C.-C.; Lu, C.-L.; Shieu, F.-S.; Shih, H.C. Structure and Photoluminescence Properties of Thermally Synthesized V_2O_5 and Al-Doped V_2O_5 Nanostructures. *Materials* **2021**, *14*, 359. https://doi.org/10.3390/ma14020359

Received: 11 December 2020
Accepted: 11 January 2021
Published: 13 January 2021

1. Introduction

Vanadium is a multi-valent element with oxidation states of V^{2+}, V^{3+}, V^{4+}, and V^{5+}, and therefore has several phase-states, including vanadium monoxide (VO), vanadium sesquioxide (V_2O_3), vanadium dioxide (VO_2), and vanadium pentoxide (V_2O_5) [1,2]. Vanadium pentoxide (V_2O_5) is the most stable phase; it has an orthorhombic structure and layered VO_5 structures of square pyramids that share corners and edges [3,4]. The layered structure results in the V3d split-off conduction band so that V_2O_5 has direct and indirect band gaps at 2.3 and 1.9 eV [5]. Oxygen vacancies (V_O) are the most common defects in V_2O_5, and especially in the oxygen layer in the layered VO5 structure [6]. The conduction band that has split off and the V_O-defects provide a flexible pathway for luminescence. Doping with elements and the formation of the core-shell nanostructures modify the photoluminescence properties [7,8]. Many works have reported upon methods of fabricating V_2O_5, which are: atomic layer chemical vapor deposition [9], the sol-gel process [10], thermal deposition [11], the hydrothermal process [12], and the thermal evaporation process [7,8]. The photoluminescence property of V_2O_5 can be modified by the different dopants, such as Er [13], Co [14], Nd [15,16], Gd [16]; Al [10], and Ga [7]. The above doped V_2O_5 materials possess potential applications in light emitters, photocatalysts, and cathodic materials for ionic batteries. Owing to the layered structures and tunable photoluminescence properties, V_2O_5 has many applications, including electrochromic devices [17], solar cells [18,19], catalysts [20], solid-state batteries [21], gas sensors [22], chemical species sensors [23], smart windows [4], etc. The dopants as mentioned above were not metallic powders. Instead, the nitrate [10,13,15], sulfate [14], and oxide powders [16] were the dopants, which implied that the metallic ions were easy to form during the synthesized process, resulting in the subsequent influence in photoluminescence. However, the zero-valent metallic ion can also show the influence in the photoluminescence

property. Compared to previous literature [7,10,13–16], this work shows for the first time the metallic Al powders acting as dopants and doping V_2O_5 nanostructures. This implies that the zero-valent and/or tri-valent Al ions can be observed, and their influence in the photoluminescence property of the V_2O_5 nanostructures can be studied. Al-doped V_2O_5 shows potential applications including as photodiode [24], in electrocatalysis [25], thin-film batteries [26], and as cathodic materials for lithium ion batteries [10].

In this work, metallic Al powder was directly used as a source of metallic Al dopant. Both Al-free and Al-doped V_2O_5 nanostructures (NSs) were fabricated on Si(100) substrate using a thermal-chemical vapor deposition (CVD) process via a catalyst-free vapor-solid (V-S) mechanism at 850°C under 1.2×10^{-1} Torr. In addition, Ar gas was introduced during the whole synthesized process to lower the oxygen partial pressure and to prevent the formation of the Al_2O_3 phase. The effects of Al doping on the crystal structures, binding energies, bonding vibration modes, and luminescence properties of V_2O_5 NSs are systematically analyzed based on the results of X-ray diffraction (XRD), high-resolution transmission electron microscopy (HRTEM), and Raman, and photoluminescence spectra.

2. Materials and Methods

2.1. Fabrication of Al-Free and Al-Doped V_2O_5 Nanostructures

Al-free V_2O_5 NSs were deposited on the Si (100) substrates by the catalyst-free V-S mechanism using the thermal-CVD process at 850 °C in a quartz tube furnace. A 0.3 g mass of high-purity V_2O_5 powder (Aldrich, Shanghai, China, 99.5%) was placed in an alumina crucible in the center of the quartz tube; about 10cm downstream of the crucible was placed the Si (100) substrate. The system pressure was pumped down to 4.0×10^{-2} Torr and the temperature was increased to 850 °C at 25 °C/min in Ar 30 standard cubic centimeter per minute (sccm) V_2O_5 powder was evaporated at 850 °C for 1.5 h, and its vapor was mixed with Ar (30 sccm) and O_2 (20 sccm) at 1.2×10^{-1} Torr; V_2O_5 NSs were grown on Si(100) substrate and then cooled to room-temperature at 30 sccm Ar. The final products were denoted as AV0 NSs. Al-doped V_2O_5 NSs were synthesized in a similar manner. The starting materials were a mixture of 0.3 g powdered V_2O_5 with various amounts of powdered Al (Aldrich, 99.9%)—1.5 mg (0.5 wt.%), 3 mg (1 wt.%), and 4.5 mg (1.5 wt.%)—that were co-evaporated at 850 °C to yield AV05, AV10, and AV15, respectively.

Before analyzing processes, all samples were preserved in a glass desiccator under the pressure of 1 Torr. The samples of the AV nanostructures being covered on the Si(100) substrates were directly analyzed using XRD, X-ray photoelectron spectroscopy (XPS), field-emission scanning electron microscopy (FESEM), Raman, and photoluminescence (PL). The AV nanostructures were detached from the Si(100) substrate by ultrasonication in the ethanol solution, followed by the HRTEM observation.

2.2. Characterizations

The crystal structures of the AV NSs were determined using a mass absorption coefficient glancing incident X-ray diffractometer with Cu kα radiation source (λ = 0.154 nm, 40 kV, 30 A, Bruker D2 PHASER) in the recording range from 20 to 60° and high-resolution transmission electron microscope with the electron accelerating voltage of 200 kV (HRTEM, JEOL, JEM-3000F, Tokyo, Japan). The chemical binding energies were measured by X-ray photoelectron spectroscope using the Al kα radiation with the electron energy of 1486.6 eV (XPS, Perkin-Elmer model PHI1600 system, Waltham, MA, USA). The chemical bonding vibration modes were identified by Raman spectrometer (3D Nanometer Scale Raman PL microspectrometer, Tokyo Instruments, INC., Tokyo, Japan) with an excitation source of a semiconductor laser at the wavelength of 532 nm. Room-temperature PL spectra were recorded by a confocal Raman spectrometer (Alpha300, Witec, Ulm, Germany) with the source of semiconductor laser (λ = 532 nm, 0.5 mW).

3. Results

3.1. X-ray Photoelectron Spectroscopy (XPS) Analysis

Figure 1a presents the XPS spectra of the V 2p and O 1s orbitals of AV0 and AV15 NSs. The peaks at 516.4 eV (V $2p^{3/2}$) and 523.7 eV (V $2p^{1/2}$) of the AV0 NSs with a splitting Δ-value of 7.3 eV are consistent with the characteristic of orthorhombic V_2O_5 structures [27]. The AV15 NSs show a similar splitting Δ-value (7.4 eV), indicating that the Al dopants do not affect the V_2O_5 orthorhombic structure. The O 1s peak at 529.3 eV is attributed to the oxygen ions (O_L) associated with the V–O bonds in the V_2O_5 structures [28,29]; the peak at 530.7 eV (O_C) is attributed to the chemisorbed oxygen on the surface of the NSs [7]. The energy difference between V $2p^{3/2}$ and O_L is about 12.9 eV, indicating the formation of the V_2O_5 phase [29]. The values of V 2p and O_L in the AV15 NSs (Figure 1a) are similar to those of the AV0 NSs. However, the binding energy of O_C in AV15 NSs shifts upward to 532.2 eV relative to that of AV0 NSs (530.7 eV). The reduction potential of Al is as low as −0.677 V [30], indicating that Al more easily reacts with oxygen-containing species, such as oxygen and/or hydroxyl, and forms the amorphous phases of Al–O and/or Al–OH [31] at the surface of the NSs.

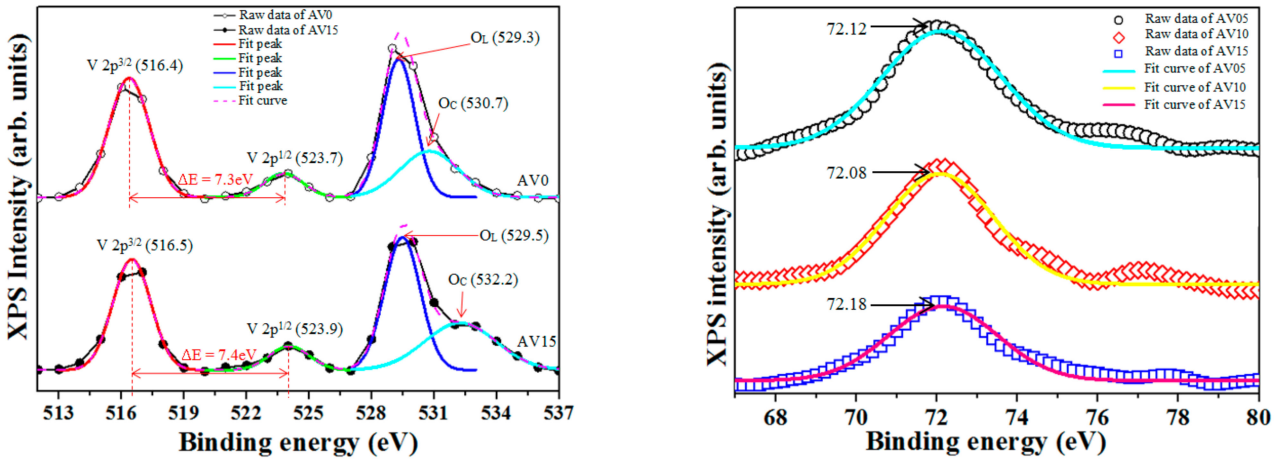

Figure 1. X-ray photoelectron spectroscopy (XPS) spectra of V 2p and O 1s of (**a**) AV0 and AV15 NSs (Al-doped V_2O_5 nanostructures). (**b**) Al 2p of AV NSs.

Therefore, the O_C position in AV15 NSs ends up with a blue-shift. Figure 1b shows that the energies of the Al 2p orbitals in AV05, AV10, and AV15 NSs have the same binding energy of 72.12 eV [32], showing that the Al dopants behave as a metal rather than the ions in the V_2O_5 NSs. Table 1 presents the atomic percentage (at.%) of Al in the V_2O_5 NSs, indicating that the at.% of Al dopant increases with Al contents.

Table 1. Al at.% of the AV NSs with various Al contents (wt.%).

Samples	AV0	AV05	AV10	AV15
Al contents(g)	0	0.0015	0.003	0.0045
Al contents (wt.%)	0	0.5	1	1.5
Al contents (at.%)	0	4.45	8.64	11.31

3.2. X-ray Diffraction (XRD) Patterns

The powder XRD analysis of both Al-free and Al-doped V_2O_5 NSs reveal the typical orthorhombic V_2O_5 structure (joint committee on powder diffraction standard (JCPDS) 77-2418) with the planes (001), (110), (400), (111), (002), and (600) at diffraction angles of 20.36, 26.16, 31.06, 33.01, 41.37, and 47.35°, correspondingly, as presented in Figure 2.

No irrelevant phases, such as Al_2O_3 and metallic Al, were detected. The insets in Figure 2a reveal that the full width at half maximum (FWHM) of the V_2O_5 (001) plane varies with the Al content and show a deviation of ±2.9% of all the AV NSs, indicating that the Al dopants do not affect the V_2O_5 crystal structure.

Based on the Bragg law and the plane-spacing equation for an orthorhombic structure, $\frac{1}{d_{hkl}^2} = \frac{h^2}{a^2} + \frac{k^2}{b^2} + \frac{l^2}{c^2}$, the lattice constants (a, b, and c), and the ratios c/a and c/b can be estimated; they are provided in Table 2. Both c/a and c/b ratios increase with the addition of Al dopant, as shown in Figure 2b. The V_2O_5 comprises packed layered [VO_5]–[VO_5] structures, facilitating the formation of V_O between the layers [8,11]. The radius of the Al^0 is 1.43 Å similar to the V_O(1.4 Å). The interlayer spacing of the layered V_2O_5 structure is about 4.32 Å [33].

Table 2. Lattice constants, c/a, and c/b of the AV NSs with various Al contents.

Al Contents (wt.%)	Diffraction Angle (2θ)			Lattice Constants of V_2O_5 (Å)			c/a	c/b
	V_2O_5 (001)	V_2O_5 (110)	V_2O_5(400)	a	b	c		
0	20.36	26.17	31.07	11.504	3.562	4.357	0.3787	1.2234
0.5	20.42	26.28	31.19	11.461	3.546	4.345	0.3791	1.2253
1.0	20.35	26.19	31.10	11.492	3.558	4.361	0.3795	1.2256
1.5	20.33	26.19	31.09	11.494	3.558	4.363	0.3842	1.2263

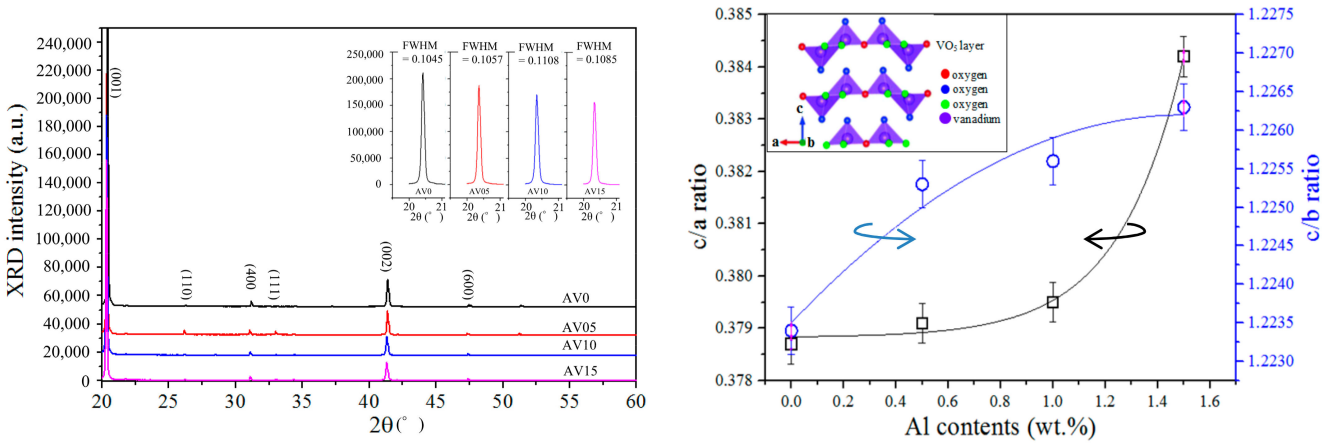

(**a**) (**b**)

Figure 2. (**a**) Powder X-ray diffraction (XRD) analysis of AV NSs and the inset showing FWHMs varying Al dopants in V_2O_5 (001); (**b**) c/a and c/b ratios varying with Al dopant (wt.%); the inset depicting the V_2O_5 molecular structures [34].

Therefore, the increase in c/a and c/b can be attributed to the filling by Al^0 of the sites of V_O and/or intercalating between the two layered VO_5 structures in V_2O_5 NSs. The Al dopant slightly increases the lattice distance between the two [VO_5]-layers in the a–c plane (inset in Figure 2b [34]) by approximately 0.1–0.2% when the Al content is ≤1 wt.% and a more significant increase of the lattice distance (by 1.2%) at an Al-dopant content of 1.5 wt.%. The lattice spacing in the a–b plane (inset in Figure 2b [34]) significantly increases with the incorporation of Al dopant. These results reveal that the c/b and c/a ratios increase with the incorporated Al dopants in the V_2O_5 NSs.

3.3. Field-Emission Scanning Electron Microscopy (FESEM) and High-Resolution Transmission Electron Microscopy (HRTEM) Analysis

FESEM images of AV0 and AV10 NSs are shown in Figure 3a,b. Most of the nanostructures exhibit the nanowire-like shape. Their crystal structure and growth direction are

estimated by the following HRTEM analysis and shown in Figure 3c,d. Inset 1 (Figure 3c) shows d-spacings of 5.7 and 3.6 Å, consistent with the planes V_2O_5 (100) and V_2O_5 (110); the angle between the (100) and (110) planes is 72°, consistent with the selective area diffraction (SAD) pattern in inset 2 (Figure 3c). The d-spacings of AV10 NSs, as shown in inset 3 (Figure 3d), are 4.2 and 3.4 Å, consistent with the planes V_2O_5 (001) and V_2O_5 (110) and the angle between (001) and (110) is 89.5°, consistent with the SAD pattern in inset 4 (Figure 3d). The theoretical angles between (110) and (200) and between (110) and (001) are 73° and 90°, respectively, which are estimated using the formula, $\phi = cos^{-1}\left[\frac{\frac{h_1h_2}{a^2}+\frac{k_1k_2}{b^2}+\frac{l_1l_2}{c^2}}{\sqrt{\left(\frac{h_1^2}{a^2}+\frac{k_1^2}{b^2}+\frac{l_1^2}{c^2}\right)\left(\frac{h_2^2}{a^2}+\frac{k_2^2}{b^2}+\frac{l_2^2}{c^2}\right)}}\right]$, where ϕ is the angle between the ($h_1k_1l_1$) plane and the ($h_2k_2l_2$) plane; a (11.51 Å), b (3.559 Å), and c (4.371 Å) are the lattice constants of the orthorhombic V_2O_5 structure Based on the above discussion, the growth direction of the AV NSs can thus be confirmed as being in the [110]-direction.

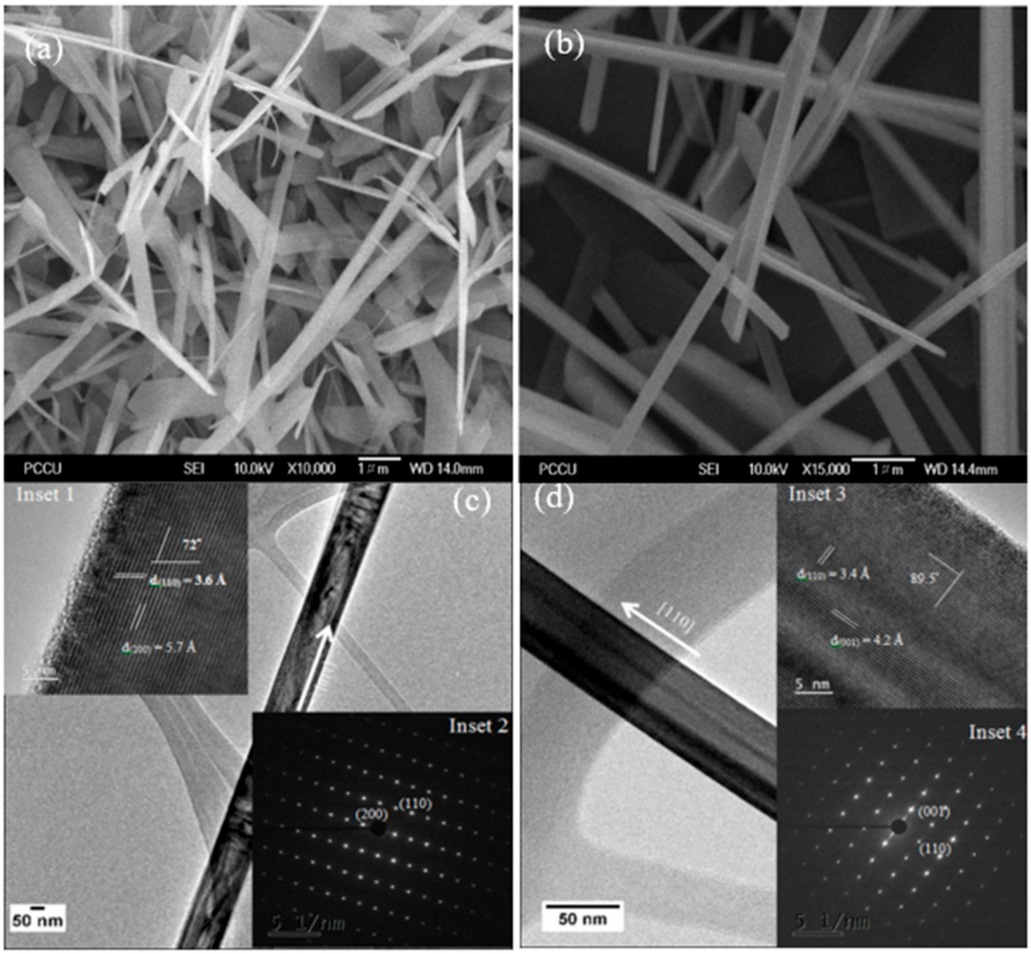

Figure 3. Field-emission scanning electron microscopy (FESEM) images of (**a**) AV0 and (**b**) AV10 nanostructures. High-resolution transmission electron microscopy (HRTEM) images of (**c**) AV0 and (**d**) AV10 NSs, Insets 1 and 3 showing the high resolution images of the AV0 and AV10 NSs, respectively; while inset 2 and 4 showing the SAD pattern of the AV0 and AV10 NSs.

3.4. Raman Spectra

The V_2O_5 structure is orthorhombic and has a P_{mnm} symmetry; V_2O_5 has typical Raman active peaks of AV0 and AV10 NSs which fitted by Gaussian deconvolution are observed at around 141.71, 195.26, 282.04, 302.64, 403.51, 480.45, 524.80, 699.93, and 993.36 cm^{-1} [3,35–37], as shown Figure 4a and listed in Table 3. The crystal structure

of V_2O_5 NSs is layered V_2O_5s that is packed along the c-axis of the unit cell, and each V_2O_5 layer comprises square pyramids of VO_5 that share edges and corners, as shown in Figure 4b [8,38]. One vanadium atom is connected to six oxygen atoms with five bond lengths, which are of 1.557, 1.779, 1.878, 2.017, and 2.791 Å, as shown schematically in Figure 4b [38]. The V–O1 bond has the strongest binding energy but the shortest bonding length (1.557 Å) of all of the V–O bonds; the V–O1′ bond is a weak Van der Waals' bond between layered-VO_5 with a bonding length of 2.791 Å; along the b-axis, the V–O21 and V–O22 bonds have a length of 1.878 Å; along the a-axis, the V–O bonds are of two types:

(1) The V–O2′1 bond has a length of 2.017 Å, and
(2) The V–O3 bond has a length of 1.779 Å.

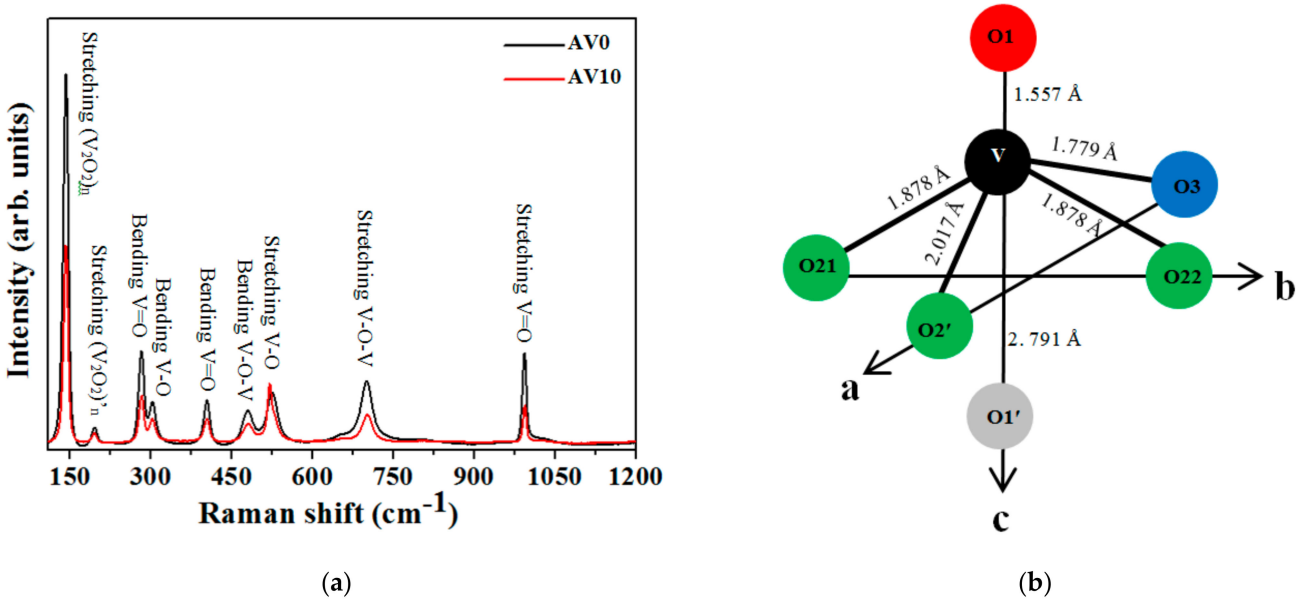

(**a**) (**b**)

Figure 4. (**a**) Raman spectra of the AV0 and AV10 NSs, and (**b**) schematic V_2O_5 molecular Scheme [38].

Table 3. Characteristic Raman shifts of the nanostructures of AV0 and AV10 NSs.

Raman Scattering Modes	AV0 NSs		AV10 NSs		Deviation of the Raman Shifts (%)
	Raman Shifts (cm^{-1})	Intensity	Raman Shifts (cm^{-1})	Intensity	
Stretching $(V_2O_2)_n$	141.71	84,745.82	141.93	45,097.12	0.071
Stretching $(V_2O_2)'_n$	195.26	3371.40	194.45	1830.32	0.051
Bending V=O	282.04	20,894.35	282.14	10,431.08	0.017
Bending V–O	302.64	9033.58	302.47	5007.98	0.016
Bending V=O	403.51	9475.78	403.33	4967.71	0.025
Bending V–O–V	480.45	6944.95	481.35	3846.47	0.062
Stretching V–O	524.80	11,097.60	522.07	11,202.89	0.258
Stretching V–O–V	699.93	12,863.33	701.25	5757.458	0.099
Stretching V=O	993.36	20,228.08	994.02	8188.87	0.030

This orthorhombic V_2O_5 structure has two bonding vibrations. They are: (1) stretching mode: the terminal oxygen of the V=O bond is the unshared oxygen (O1) and yields a peak at 993.36 cm^{-1} [39,40]; the doubly coordinated oxygen in the V–O–V bond is a corner-sharing oxygen in one of the two adjacent pyramids yields a peak at 699.93 cm^{-1} [41]; the triply coordinated oxygen of the V–O bond is an edged-sharing oxygen in three adjacent pyramids yields a peak at 524.80 cm^{-1} [6,39]; and (2) bending mode: the bridging V–O–V

bond at 480.45 cm^{-1} [39,41]; the terminal oxygen associated with the V=O bond yields a peak at 403.51 cm^{-1} [40]; the triply coordinated oxygen associated with the V–O bond yields a peak at 302.64 cm^{-1} [6]; the V=O terminal oxygen associated with the bond yields a peak at 282.04 cm^{-1}; $(V_2O_2)_n$ and $(V_2O_2)'_n$ bonds yield peaks at 194.26 and 141.71 cm^{-1}, respectively, corresponding to the chain translation and strongly associated with the layered structures [41]. Table 3 presents the Raman shifts of the AV0 and AV10 NSs. The deviations of the Raman shifts upon the addition of Al reveal a slight difference between AV0 and AV10 NSs, indicating that Al has no major effect on the V_2O_5 binding structures, which is consistent with the XPS results.

The intensity of the Raman peaks (as shown in Figure 4a and Table 3) clearly decreases upon the addition of Al dopant. Jung et al. [42] reported a decrease in the Raman intensity from V_2O_5 upon the insertion of Li into the $Li_xV_2O_5$ lattice owing to the formation of negative charge carriers by the reduction of V^{5+} to V^{4+} [43]; Park et al. determined that the decreasing Raman intensity is attributable to the extraction of Li from the Li_xCoO_2 lattice because the oxidization state increases from Co^{3+} to Co^{4+}, generating positive charge carriers [44,45]. Both of these cases are attributable to the metallization of the host materials, so decreases in Raman intensity arise from the reduction of the optical skin depth of the Raman excitation light [42]. In this work, metallic Al is doped into the V_2O_5 lattice, as revealed by XPS and XRD; the host materials, therefore, exhibit more metallic characters. Hence, the Raman intensity of the V_2O_5 NSs clearly decreases with the addition of Al (Figure 4a).

3.5. Photoluminescence (PL) Spectra

Figure 5a presents the PL spectra of the AV NSs, which reveal two prominent emissions at 1.77 (E1) and 1.94 eV (E2). V_2O_5 has split-off conduction bands owing to its layered structure, suggesting that it has several energy bands from the top of the O2p valance band to the split-off V3d conduction band [11]. The V_2O_5 crystal structure comprises from the $[VO_5]$-$[VO_5]$ layers and oxygen vacancies (V_O) easily being formed between the layers [11]. Accordingly, the V_O-related emission E1 occurs at 1.77 eV and E2 at 1.94 eV is attributed to the intrinsic emission band, which is split off from the V3d conduction band in the V_2O_5 NSs [6,46]. Figure 5b presents variations of the intensities of E1 and E2 with the Al content. Such variations in luminescence intensities decay exponentially as Al content increases. The intensity of E1 decreases by about 61.6% and that of E2 decreases by about 59.9% as the Al content increases from 0 to 1.5 wt.%.

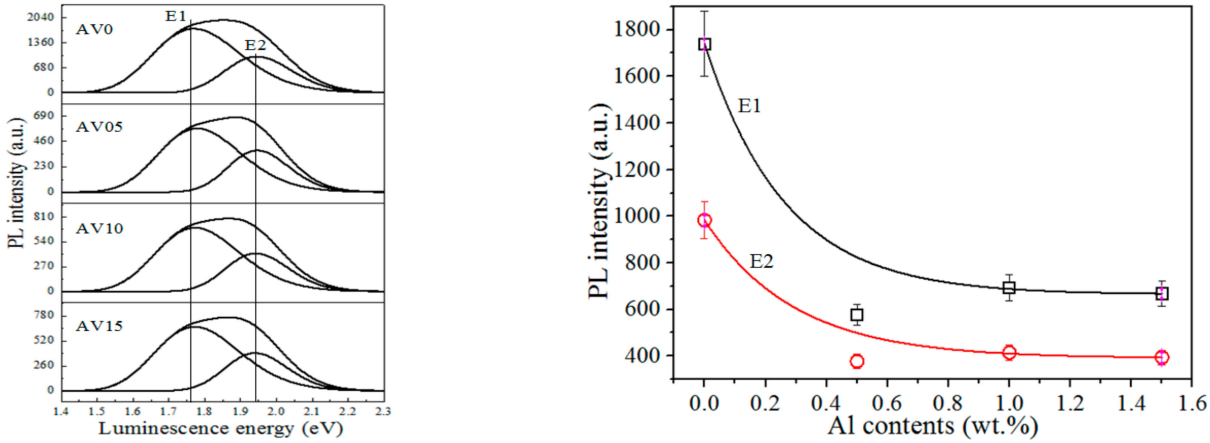

(**a**) (**b**)

Figure 5. (**a**) Photoluminescence (PL) spectra of the samples AV0, AV05, AV10, and AV15 NSs; and (**b**) intensities of the E1 and E2 varying with the Al contents.

Table 4 shows the influence in the photoluminescence intensity of the V_2O_5 by different dopants, including metallic Al, metallic Ga [7], aluminum nitrate nonahydrate ($Al(NO_3)_3 \cdot 9H_2O$) [10], erbium nitrate pentahydrate ($Er(NO_3)_3 \cdot 5H_2O$) [13], cobalt sulfate heptahydrate ($CoSO_4 \cdot 7H_2O$) [14], gadolinium oxide (Gd_2O_3) [16], neodymium oxide (Nd_2O_3) [16], aluminum nitrate ($Al(NO_3)_3$) [24], and aluminium oxide (Al_2O_3) [26]. Besides the Ga dopants, the PL intensities of V_2O_5 decrease with the zero-valent Al the same as the results of the tri-valent elements.

Table 4. The influence in PL intensities of V_2O_5 in various dopant precursors.

Dopant Precursors	Dopant Type	PL Intensity of the V_2O_5	Ref.
metallic Al	Al^0	Decreases with the increasing precursor contents	This work
metallic Ga	Ga^{3+}	Enhancement at proper precursor contents	[7]
$Al(NO_3)_3 \cdot 9H_2O$	Al^{3+}	Decreases with the increasing precursor contents	[10]
$Er(NO_3)_3 \cdot 5H_2O$	Er^{3+}	No data	[13]
$CoSO_4 \cdot 7H_2O$	Co^{2+}	Decreases with the increasing precursor contents	[14]
Gd_2O_3	Gd^{3+}	Decreases with the adding of precursor	[16]
Nd_2O_3	Nd^{3+}	Decreases with the adding of precursor	[16]
$Al(NO_3)_3$	Al^{3+}	Decreases with the adding of precursor	[24]

3.6. Proposed Luminescence Mechanism

Figure 6 presents a possible mechanism for E1 and E2 from the AV NSs. The conduction band (E_C), Fermi level (E_F), and valence band (E_V) of the V_2O_5 structures in the Al-free V_2O_5 NSs, are at −4.7, −5.45, and −7.00 eV [47], respectively, as shown in Figure 6a. Some of the excited electrons in the E1 level were generated by an incident light from the E_v of the V_2O_5 transiting to the E2 level, causing the intensity of E2 to exceed that of E1, as shown in Figure 5b. According to XPS and XRD results, the metallic Al exists in the V_2O_5 NSs, which can be located between the layered V_2O_5 structure and/or the oxygen vacancy. The Fermi level of the metallic Al is approximately 4.08–4.28 eV [48]. Hence, in the Al-doped V_2O_5 NSs, as shown in Figure 6b, these excited electrons in the E2 level, which were excited by the incident radiation, can transit along three pathways. These pathways are (1) from E2 to E1, and then to the Fermi level of the metallic Al; (2) from E2 to the work-function level of the metallic Al; and (3) from E2 to E1. Along pathway 1, the excited electrons transit to the metallic Al, so the E2 intensity decreases; along pathway 2, the electrons that are generated upon the formation of the V_O-defects transit to the metallic Al, leading the decreasing E1 intensity; along pathway 3, the excited electrons in the E2 level transit to the E1 level, so the intensity of E2 is lower than that of E1 for all of the AV NSs. Moreover, the concentration of V_O is reduced upon the addition of Al dopant because the sites of the V_O defects are filled by Al^0. Then the intensity of E1 emission thus tends to decrease. These results suggest that Al as the dopant plays the following three roles in the AV NSs system: (1) as an electron sink, (2) filling the sites of the V_O defects and reducing the V_O concentration, and (3) intercalating the layered V_2O_5 structure. Therefore, the intensity of E1 and E2 both decreases as the Al dopant concentration increases.

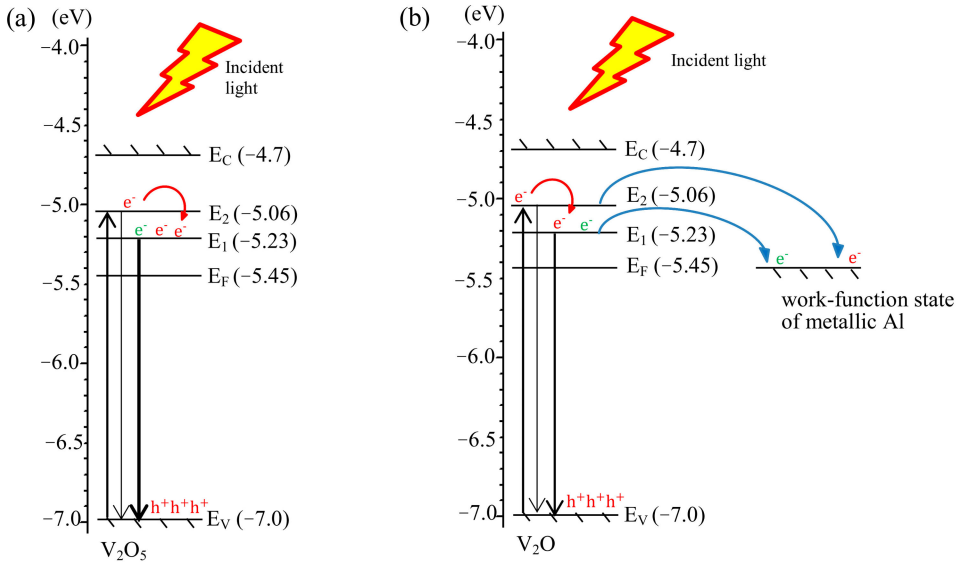

Figure 6. Proposed mechanism of the migration pathways for the electrons and holes in (**a**) Al-free and (**b**) Al-doped V_2O_5 NSs at an equilibrium state.

4. Conclusions

Both Al-free and Al-doped V_2O_5 NSs were fabricated on the Si (100) substrate by a thermally activated CVD process at 850 °C via a V-S mechanism. XPS revealed the V–O binding energy of the V_2O_5 phase and the presence of metallic Al rather than Al^{3+} ions. XRD revealed the typical orthorhombic phase of the V_2O_5 with c/a and c/b ratios that increase with the Al dopant concentration, suggesting that Al^0 (radius = 1.43 Å) preferentially fills the V_O (radius = 1.4 Å) sites owing to their similar sizes. The FWHM has a similar value with a deviation of ±2.9% upon the addition of Al dopant, indicating that Al does not affect the V_2O_5 crystal structure. HRTEM verified that the growth direction of both Al-free and Al-doped V_2O_5 NSs is in the [110]-direction. Raman shifts revealed slight deviations upon the addition of Al, indicating that the Al content does not affect the binding structure of the V_2O_5. The photoluminescence results proved that the emission intensities at 1.77 and 1.94 eV decreased by factors of 61.6% and 59.9%, respectively, as the concentration of Al dopant increases from 0 to 1.5 wt.%. The decrease in the luminescence intensities was attributable to the following causes: (1) Al dopants reduced the V_O-defect concentration and (2) Al acted as an electron sink. Therefore, the recombination rate of electrons and holes decreases, reducing the luminescence intensities at 1.77 and 1.94 eV, upon doping with Al. Al-doped V_2O_5 NSs have potential applications in photocatalysts, solar cells, gas sensors, and electrodic materials.

Author Contributions: Conceptualization, H.C.S. and F.-S.S.; methodology, H.C.S., F.-S.S., C.-L.L. and C.-C.W.; software, C.-C.W. and C.-L.L.; validation, C.-C.W. and C.-L.L.; formal analysis, C.-C.W.; investigation, C.-C.W., and C.-L.L.; resources, H.C.S. and F.-S.S.; data curation, C.-C.W. and C.-L.L.; writing—original draft preparation, C.-C.W.; writing—review and editing, H.C.S. and F.-S.S.; visualization, C.-C.W. and C.-L.L.; supervision, H.C.S. and F.-S.S.; project administration, H.C.S.; funding acquisition, H.C.S. All authors have read and agreed to the published version of the manuscript.

Funding: This research was funded by the Ministry of Science and Technology (MOST) of Taiwan, Republic of China, grant number MOST 108-2221-E-034-010.

Institutional Review Board Statement: Not applicable.

Informed Consent Statement: Not applicable.

Data Availability Statement: Data is contained within the article.

Acknowledgments: The authors gratefully acknowledge the financial support of the Ministry of Science and Technology (MOST) of Taiwan.

Conflicts of Interest: The authors declare no conflict of interest.

References

1. Liu, M.; Su, B.; Tang, Y.; Jiang, X.; Yu, A. Recent advances in nanostructured vanadium oxides and composites for energy conversion. *Adv. Energy Mater.* **2017**, *7*, 1–34.
2. Surnev, S.; Ramsey, M.G.; Netzer, F.P. Vanadium oxide surface studies. *Prog. Surf. Sci.* **2003**, *73*, 117–165. [CrossRef]
3. Lee, S.H.; Cheong, H.M.; Seong, M.J.; Liu, P.; Tracy, C.E.; Mascarenhas, A.; Pitts, J.R.; Deb, S.K. Raman spectroscopic studies of amorphous vanadium oxide thin films. *Solid State Ion.* **2003**, *165*, 111–116. [CrossRef]
4. Sucharitakul, S.; Ye, G.; Lambrecht, W.R.L.; Bhandari, C.; Gross, A.; He, R.; Poelman, H.; Gao, X.P.A. V_2O_5: A 2D van der Waals oxide with strong in-plane electrical and optical anisotropy. *ACS Appl. Mater. Interfaces* **2017**, *9*, 23949–23956. [CrossRef] [PubMed]
5. Chakrabarti, A.; Hermann, K.; Druzinic, R.; Witko, M.; Wagner, F.; Petersen, M. Geometric and electronic structure of vanadium pentoxide: A density functional bulk and surface study. *Phys. Rev. B* **1999**, *59*, 10583–10590. [CrossRef]
6. Wang, Y.; Su, Q.; Chen, C.H.; Yu, M.L.; Han, G.J.; Wang, G.Q.; Xin, K.; Lan, W.; Liu, X.Q. Low temperature growth of vanadium pentoxide nanomaterials by chemical vapour deposition using VO $(acac)_2$ as precursor. *J. Phys. D Appl. Phys.* **2010**, *43*, 185102. [CrossRef]
7. Wang, C.C.; Lu, C.L.; Shieu, F.S.; Shih, H.C. Enhanced photoluminescence properties of Ga-Doped V_2O_5 nanorods via defect structures. *Chem. Phys. Lett.* **2020**, *738*, 136864. [CrossRef]
8. Wang, C.C.; Chen, K.C.; Shieu, F.S.; Shih, H.C. Characterization and photoluminescence of V_2O_5@Pt core-Shell nanostructures as fabricated by atomic layer deposition. *Chem. Phys. Lett.* **2019**, *729*, 24–29. [CrossRef]
9. Van, K.L.; Groult, H.; Mantoux, A.; Perrigaud, L.; Lantelme, F.; Lindstrom, R.; Badour-Hadjean, R.; Zanna, S.; Lincot, D. Amorphous vanadium oxide films synthesised by ALCVD for lithium rechargeable batteries. *J. Power Sources* **2006**, *160*, 592–601. [CrossRef]
10. Venkatesan, A.; Chandar, N.R.K.; Pradeeswari, K.; Pandi, P.; Kandasamy, A.; Kumar, R.M.; Jayavel, R. Influence of Al doping on structural, luminescence and electrochemical properties of V_2O_5 nanostructures synthesized via non-Hydrolytic sol-Gel technique. *Mater. Res. Express* **2019**, *6*, 015017. [CrossRef]
11. Díaz-Guerra, C.; Piqueras, J. Structural and cathodoluminescence assessment of V_2O_5 nanowires and nanotips grown by thermal deposition. *J. Appl. Phys.* **2007**, *102*, 084307. [CrossRef]
12. Schlecht, U.; Knez, M.; Duppel, V.; Kienle, L.; Burghard, M. Boomerang-shaped VOX belts: Twinning within isolated nanocrystals. *Appl. Phys. A: Mater. Sci. Process.* **2004**, *78*, 527. [CrossRef]
13. González-Rivera, Y.A.; Cervantes-Juárez, E.; Aquino-Meneses, L.; Lozada-Morales, R.; Jiménez-Sandoval, S.; Rubio-Rosas, E.; Agustín-Serrano, R.; de la Cerna, C.; Reyes-Cervantes, E.; Zelaya Angel, O.; et al. Photoluminescence in Er-Doped V_2O_5 and Er-doped CdV2O6. *J. Lumin.* **2014**, *155*, 119–124. [CrossRef]
14. Suresh, R.; Giribabu, K.; Manigandan, R.; Munusamy, S.; Kumar, S.P.; Muthamizh, S.; Stephen, A.; Narayanan, V. Doping of Co into V_2O_5 nanoparticles enhances photodegradation of methylene blue. *J. Alloys Compd.* **2014**, *598*, 151–160. [CrossRef]
15. Aquino-Meneses, L.; Lozada-Morales, R.; del Angel-Vicente, P.; Percino-Picazo, J.C.; Zelaya-Angel, O.; Becerril, M.; Carmona-Rodriguez, J.; Rodriguez-Melgarejo, F.; Jime'nez-Sandoval, S. Photoluminescence in Nd-Doped V_2O_5. *J. Mater. Sci.* **2014**, *49*, 2298–2302. [CrossRef]
16. Venkatesan, A.; Chandar, N.R.K.; Kandasamy, A.; Chinnu, M.K.; Marimuthu, K.N.; Kumar, R.M.; Jayavel, R. Luminescence and electrochemical properties of rare earth (Gd, Nd) doped V_2O_5 nanostructures synthesized by a non-Aqueous sol-Gel route. *RSC Adv.* **2015**, *5*, 21778. [CrossRef]
17. Azevedo, C.F.; Balboni, R.D.C.; Cholant, C.M.; Moura, E.A.; Lemos, R.M.J.; Pawlicka, A.; Gündel, A.; Flores, W.H.; Pereira, M.; Avellaneda, C.O. New thin films of NiO doped with V_2O_5 for electrochromic Applications. *J. Phys. Chem. Solids* **2017**, *110*, 30–35. [CrossRef]
18. Ongul, F. Solution-Processed inverted organic solar cell using V_2O_5 hole transport layer and vacuum free EGaIn anode. *Opt. Mater.* **2015**, *50*, 244–249. [CrossRef]
19. Alsulami, A.; Griffin, J.; Alqurashi, R.; Yi, H.; Iraqi, A.; Lidzey, D.; Buckley, A. Thermally stable solution processed vanadium oxide as a hole extraction layer in organic solar cells. *Materials* **2016**, *9*, 235. [CrossRef]
20. Zhao, W.; Zhong, Q.; Pan, Y.; Zhang, R. Defect structure and evolution mechanism of O^{2-} radical in F-Doped V_2O_5/TiO_2 catalysts. *Colloids Surf. A: Physicochem. Eng. Asp.* **2013**, *436*, 1013–1020. [CrossRef]
21. Pandey, G.P.; Liu, T.; Brown, E.; Yang, Y.; Li, Y.; Sun, X.S.; Fang, Y.; Li, J. Mesoporous hybrids of reduced graphene oxide and vanadium pentoxide for enhanced performance in lithium-Ion batteries and electrochemical capacitors. *ACS Appl. Mater. Interfaces* **2016**, *8*, 9200–9210. [CrossRef]
22. Mane, A.A.; Suryawanshi, M.P.; Kim, J.H.; Moholkar, A.V. Superior selectivity and enhanced response characteristics of palladium sensitized vanadium pentoxide nanorods for detection of nitrogen dioxide gas. *J. Colloid Interface Sci.* **2017**, *495*, 53–60. [CrossRef] [PubMed]
23. Ghanei-Motlagh, M.; Taher, M.A.; Fayazi, M.; Baghayeri, M.; Hosseinifar, A. Non-Enzymatic amperometric sensing of hydrogen peroxide based on vanadium pentoxide nanostructures. *J. Electrochem. Soc.* **2019**, *166*, B367–B372. [CrossRef]
24. Pradeep, I.; Kumar, E.R.; Suriyanarayanan, N.; Mohanraj, K.; Srinivas, C.; Mehar, M.V.K. Effect of Al doping concentration on the structural, optical, morphological and electrical properties of V_2O_5 nanostructures. *New J. Chem.* **2018**, *42*, 4278. [CrossRef]

25. Venkatesan, A.; Chandar, N.K.; Kumar, M.K.; Arjunan, S.; Kumar, R.M.; Jayavel, R. Al3+ Doped V_2O_5 Nanostructure: Synthesis and Structural, Morphological and Optical Characterization. In Proceedings of the AIP Conference, Mumbai, India, 3–7 December 2012; Volume 1512, p. 392.
26. Ali, H.M.; Hakeem, A.M.A. Structural and optical properties of electron-Beam evapo-Rated Al_2O_3-Doped V_2O_5 thin films for various applications. *Phys. Status Solidi A* **2010**, *207*, 132–138. [CrossRef]
27. De Jesus, L.R.; Horrocks, G.A.; Liang, Y.; Parija, A.; Jaye, C.; Wangoh, L.; Wang, J.; Fischer, D.A.; Piper, L.F.J.; Prendergast, D.; et al. Mapping polaronic states and lithiation gradients in individual V_2O_5 nanowires. *Nat. Commun.* **2016**, *7*, 12022. [CrossRef]
28. Wu, Q.H.; Thissen, A.; Jaegermann, W.; Liu, M. Photoelectron spectroscopy study of oxygen vacancy on vanadium oxides surface. *Appl. Surf. Sci.* **2004**, *236*, 473–478. [CrossRef]
29. Silversmit, G.; Depla, D.; Poelman, H.; Marin, G.B.; De Gryse, R. Determination of the V2p XPS binding energies for different vanadium oxidation states (V^{5+} to V^{0+}). *J. Electron Spectrosc. Relat. Phenom.* **2004**, *135*, 167–175. [CrossRef]
30. Harris, D.C. *Quantitative Chemical Analysis*, 7th ed.; W.H. Freeman: New York, NY, USA, 2007.
31. Sun, C.; Zeng, R.; Zhang, J.; Qiu, Z.J.; Wu, D. Effects of UV-Ozone treatment on sensing behaviours of EGFETs with Al_2O_3 sensing film. *Materials* **2017**, *10*, 1432. [CrossRef]
32. Wagner, C.D.; Riggs, W.M.; Davis, L.E.; Mullenberg, J.F. *Handbook of X-ray Photoelectron Spectroscopy*; Perkin-Elmer Corporation: Waltham, MA, USA, 1979; p. 50.
33. Murugan, A.V.; Kale, B.B.; Kwon, C.W.; Campet, G.; Vijayamohanan, K. Synthesis and characterization of a new organo–inorganic poly (3,4-ethylene dioxythiophene) PEDOT/V_2O_5 nanocomposite by intercalation. *J. Mater. Chem.* **2001**, *11*, 2470–2475. [CrossRef]
34. Singh, B.; Gupta, M.K.; Mishra, S.K.; Mittal, R.; Sastry, P.U.; Rols, S.; Chaplot, S.L. Anomalous lattice behavior of vanadium pentaoxide (V_2O_5): X-ray diffraction, inelastic neutron scattering and ab initio lattice dynamics. *Phys. Chem. Chem. Phys.* **2017**, *19*, 17967–17984. [CrossRef] [PubMed]
35. Shen, W.J.; Sun, K.W.; Lee, C.S. Electrical characterization and Raman spectroscopy of individual vanadium pentoxide nanowire. *J. Nanoparticle Res.* **2011**, *13*, 4929–4936. [CrossRef]
36. Dewangan, K.; Sinha, N.N.; Chavan, P.G.; Sharma, P.K.; Pandey, A.C.; More, M.A.; Joag, D.S.; Munichandraiah, N.; Gajbhiye, N.S. Synthesis and characterization of self-Assembled nanofiber-bundles of V_2O_5: Their electrochemical and field emission properties. *Nanoscale* **2012**, *4*, 645–651. [CrossRef] [PubMed]
37. Urena-Begar, F.; Crunteanu, A.; Raskin, J.P. Raman and XPS characterization of vanadium oxide thin films with temperature. *Appl. Surf. Sci.* **2017**, *403*, 717–727. [CrossRef]
38. Baddour-Hadjean, R.; Pereira-Ramos, J.P. Raman microspectrometry applied to the study of electrode materials for lithium batteries. *Chem. Rev.* **2010**, *110*, 1278–1319. [CrossRef]
39. Baddour-Hadjean, R.; Golabkan, V.; Pereira-Ramos, J.P.; Mantoux, A.; Lincot, D. A Raman study of the lithium insertion process in vanadium pentoxide thin films deposited by atomic layer deposition. *J. Raman Spectrosc.* **2002**, *33*, 631–638. [CrossRef]
40. Liu, X.; Huang, C.; Qiu, J.; Wang, Y. The effect of thermal annealing and laser irradiation on the microstructure of vanadium oxide nanotubes. *Appl. Surf. Sci.* **2006**, *253*, 2747–2751. [CrossRef]
41. Chen, W.; Mai, L.; Peng, J.; Xu, Q.; Zhu, Q. Raman spectroscopic study of vanadium oxide nanotubes. *J. Solid State Chem.* **2004**, *177*, 377–379. [CrossRef]
42. Jung, H.; Gerasopoulos, K.; Alec Talin, A.; Ghodssi, R. A platform for in situ Raman and stress characterizations of V_2O_5 cathode using MEMS device. *Electrochim. Acta* **2017**, *242*, 227–239. [CrossRef]
43. Al-Assiri, M.S.; El-Desoky, M.M.; Alyamani, A.; Al-Hajry, A.; Al-Mogeeth, A.; Bahgat, A.A. Structural and transport properties of Li-intercalated vanadium pentoxide nanocrystalline films. *Philos. Mag.* **2010**, *90*, 3421–3439. [CrossRef]
44. Park, Y.; Kim, N.H.; Kim, J.Y.; Eom, I.Y.; Jeong, Y.U.; Kim, M.S.; Lee, S.M.; Choi, H.C.; Jung, Y.M. Surface characterization of the high voltage $LiCoO_2$/Li cell by X-ray photoelectron spectroscopy and 2D correlation analysis. *Vib. Spectrosc.* **2010**, *53*, 60–63. [CrossRef]
45. Milewska, A.; Świerczek, K.; Tobola, J.; Boudoire, F.; Hu, Y.; Bora, D.K.; Mun, B.S.; Braun, A.; Molenda, J. The nature of the nonmetal–Metal transition in $LixCoO_2$ oxide. *Solid State Ionics* **2014**, *263*, 110–118. [CrossRef]
46. Faggio, G.; Modafferi, V.; Panzera, G.; Alfieri, D.; Santangelo, S. Micro-Raman and photoluminescence analysis of composite vanadium oxide/poly-Vinyl acetate fibres synthesised by electro-Spinning. *J. Raman Spectrosc.* **2012**, *43*, 761–768. [CrossRef]
47. Gurulakshmi, M.; Selvaraj, M.; Selvamani, A.; Vijayan, P.; Sasi Rekha, N.R.; Shanthi, K. Enhanced visible-Light photocatalytic activity of V_2O_5/S-TiO_2 nanocomposites. *Appl. Catal. A Gen.* **2012**, *449*, 31–46. [CrossRef]
48. Kumar, B.; Kaushik, B.K.; Negi, Y.S. Perspectives and challenges for organic thin film transistors: Materials, devices, processes and applications. *J. Mater. Sci: Mater. Electron.* **2014**, *25*, 1–30.